An Asymmetric Hygroscopic Structure for Moisture-Driven Hygro-Ionic Electricity Generation and Storage

Yaoxin Zhang, Shuai Guo, Zhi Gen Yu, Hao Qu, Wanxin Sun, Jiachen Yang, Lakshmi Suresh, Xueping Zhang, J. Justin Koh, and Swee Ching Tan*

The interactions between moisture and materials give rise to the possibility of moisture-driven energy generation (MEG). Current MEG materials and devices only establish this interaction during water sorption in specific configurations, and conversion is eventually ceased by saturated water uptake. This paper reports an asymmetric hygroscopic structure (AHS) that simultaneously achieves energy harvesting and storage from moisture absorption. The AHS is constructed by the asymmetric deposition of a hygroscopic ionic hydrogel over a layer of functionalized carbon. Water absorbed from the air creates wet-dry asymmetry across the AHS and hence an in-plane electric field. The asymmetry can be perpetually maintained even after saturated water absorption. The absorbed water triggers the spontaneous development of an electrical double layer (EDL) over the carbon surface, which is termed a hygro-ionic process, accounting for the capacitive properties of the AHS. A peak power density of 70 µW cm^{-3} was realized after geometry optimization. The AHS shows the ability to be recharged either by itself owing to a self-regeneration effect or via external electrical means, which allows it to serve as an energy storage device. In addition to insights into moisture-material interaction, AHSs further shows potential for electronics powering in assembled devices.

1. Introduction

Water–materials interactions are ubiquitous and have long been a topic of constant interests across various areas.[1–4] When water meets a material, valuable information can be obtained. For example, the charge separation and migration disclosed at the water-material interface opens up possibilities for energy harvesting.[5] Prior studies have extensively investigated the types of interactions triggered by liquid water. Typical examples include the triboelectric conversion in the process of water droplets impinging onto dielectrics and the electrokinetic streaming potential that originates from fluid transport through nano- and microporous structures.[6,7] In contrast, atmospheric water, that is, water in its gaseous form, is often overlooked. It is worth noting that attempts have recently been made to explore the moisture-material interaction, which drives innovation in traditional areas, such as water splitting.[8] Hygroscopic hydrogels have been employed in recent studies as water-absorbing electrolytes to integrate with photoelectrochemical catalysts for moisture splitting.[9,10] It has also facilitated exciting progresses in a wide range of emerging areas and applications.[11–14] For example, modulating the site-specific water binding behavior of metal–organic-framework (MOF) leads to a significant improvement in atmospheric water harvesting (AWH) productivity.[15]

In particular, moisture-driven electricity generation (MEG) has attracted increasing attention. Many functional materials, such as the graphene oxide film with heterogeneous distribution of oxygen content, polymer membranes and bacterial protein nanowires, have demonstrated the ability to produce electricity on contact with humid air.[16–19] The functional groups of these materials play a key role; not only do they provide affinity sites for water sorption, especially oxygen-containing species, but also produce free charge carriers (e.g., protons) on contact with water.[7,20] The directional movement of these moisture-liberated carriers (for example, from one side of an ion-selective porous membrane to the other) drives the development of the electric field.[17] Thus, a difference in the concentration of mobile charge carriers is essential in enabling this directional diffusion for electric field generation. This is mostly achieved by creating a built-in water gradient, which can be accomplished either by asymmetric moisturisation of the active materials in a sealing device,[18] or by relying on the environmental humidity gradient.[21] Maintaining this water gradient, and hence the electric field across the active materials, is challenging, as the

Y. Zhang, S. Guo, H. Qu, J. Yang, L. Suresh, X. Zhang, J. J. Koh, S. C. Tan
Department of Materials Science and Engineering
National University of Singapore
9 Engineering drive 1, Singapore 117575, Singapore
E-mail: msetansc@nus.edu.sg
Z. G. Yu
Institute of High Performance Computing
Agency for Science, Technology and Research
1 Fusionopolis Way, Singapore 138632, Singapore
W. Sun
Division of Nano Surfaces
Bruker Corporation
11 Biopolis Way, Singapore 138667, Singapore

The ORCID identification number(s) for the author(s) of this article can be found under https://doi.org/10.1002/adma.202201228.

DOI: 10.1002/adma.202201228

**ADVANCED
SCIENCE NEWS**

www.advancedsciencenews.com

**ADVANCED
MATERIALS**

www.advmat.de

saturated water uptake eventually leads to an even water distribution. Recently, significant progress was made by demonstrating the formation of a durable built-in water gradient for long-lasting MEG output.[16–18]

However, structural limitations remain. The primary one is that the active materials cannot be freely or entirely exposed to humid air, as they would erase the interior water gradient, which would in turn fail to drive MEG conversion (Figure S1, Supporting Information).[16,22] Thus, if an environmental humidity gradient is not available, active materials must be partially sealed to maintain the desired water gradient. This would present the following shortcomings: 1) an excessive dependence on the sealing structure presents difficulties in technical feasibility; 2) even with the seal, the assembled device could still eventually lose this water gradient after saturated water uptake; and 3) the current collectors must be separated by a large distance to maintain the gradient for a sufficiently long time, but this inevitably increases the internal resistance. It is also important to note that conversion only takes place during water sorption,[18] and if an MEG material/device is left in an open environment when not in use, it would ultimately become no longer capable of power generation after its water absorption reaches saturation. Thus, barriers could arise from these limitations for the practical use of MEG materials/devices. In this regard, addressing these challenges is considered seminal, which not only pushes forward the development of MEG, but also broadens our fundamental understanding of moisture-material interactions.

We herein propound an original asymmetric hygroscopic structure (AHS) with an unusual MEG conversion route to confront the above challenges. This is accomplished by preparing a hygroscopic ionic hydrogel followed by partial deposition of the hydrogel onto a layer of functionalized carbon to construct AHS. By absorbing water from the air, wet-dry asymmetry is developed across the carbon substrate. In doing this, the polymeric network of the hydrogel firmly confines water molecules and inhibits water diffusion such that long-term exposure to moisture cannot break the asymmetry. The surface state of wet carbon undergoes dramatic variation originating from the subsequent ionic interaction between the hygroscopic hydrogel and the underlying carbon, leading to the spontaneous development of an electrical double layer (EDL) over its surface. Therefore, a durable in-plane potential difference is induced (>0.6 V) across the AHS. Moreover, the permanently maintained asymmetry allows the AHS to be freely exposed to humid environment and sustain this built-in voltage for hundreds of hours even after saturated water uptake. Here, we refer to this process as hygroionic conversion. Notably, the energy scavenged from water absorption is stored in the aggregated EDLs at the wet-dry interface, instead of being released during the absorption process, as in many MEG predecessors. Power generation by the AHS was thus carried out after water absorption was accomplished, and a peak volumetric power density of ≈70 µW cm^{-3}, which is equivalent to ≈226 µW g^{-1}, was achieved with geometry optimization. It was interestingly found that the dynamic water exchange between the AHS and the surrounding air enables the self-regeneration of it for repeated use. Such capacitive behavior also allows AHS to be further recharged via external electrical means, which demonstrates that an MEG device could also be repurposed for energy storage. Based on these innovative findings, integrated power supply unites, such as AHS-assembled penlight devices, can then be used to power small electronics. With exceptional ease of scalability (≈\$0.15 per m^2), AHSs demonstrate promising potential for the development of portable power sources and self-powered electronics, such as transistors and memristors.[23–25]

2. Results and Discussion

2.1. Architecting AHS with Permanent Wet–Dry Asymmetry

An AHS was designed by the procedure illustrated in **Figure 1**a. As the thin carbon film readily disintegrates upon contact with water owing to strong repulsion forces,[26] we chose to deposit a layer of carbon on a non-woven fabric base. The treatment was carried out by dip coating with carbon ink (Figure S2, Supporting Information), which is an aqueous dispersion of carbon black nanoparticles and a surfactant (sodium dodecyl benzene sulfonate). The primary purpose of the surfactant additive is to stabilize the dispersion and prevent the aggregation of carbon black nanoparticles (Figure S3, Supporting Information). This carbon layer endowed the fabric with electrical conductivity required for MEG conversion, and the carbon loading density determined the exact value of conductivity (Figure S4, Supporting Information). For our fabric-based AHS, 0.008 S m^{-1} was achieved at a loading density of 6 g m^{-2}, which could readily be enhanced to 0.5 S m^{-1} at 20 g m^{-2} by repeating the dip coating process. Furthermore, carbon black nanoparticles, which can be easily oxidized either during the manufacturing process or during storage in ambient air, carry abundant oxygen-containing surface functional groups (Figure S5, Supporting Information).[7,27,28] Only half of the as-fabricated carbon-coated fabric was coated with ionic hygroscopic hydrogel, leaving the other half blank. An asymmetric configuration was collectively achieved due to the opposite surface-wetting states of the two moieties after water absorption. This asymmetry was well-defined when the hydrogel and blank areas were identically shaped. The pattern of hygroscopic paint on the carbon surface could be further altered, as shown in a later section. The hydrogel was prepared by embedding deliquescent sea salt into polymeric polyvinyl alcohol (PVA). Sea salt was selected as the ionic water-absorbing compound on account of its multiple materials-related benefits and ecological sustainability (see details in the Supporting Information). Hygroscopic behavior was quantified through water sorption isotherm measurements (Figure 1b). Notably, the results indicate an exceedingly high water uptake capacity for this ionic compound of >500% of the weight of the salt compound at high relative humidity (RH). The plot also reveals that the water absorption at low and intermediate RH is less obvious but remarkably enhanced once the RH surpasses 70%. In addition to the enormous water absorption potential, another important consideration is that, the hygroscopic nature of sea salt has not previously been explored before in the field of energy for applications such as atmospheric water harvesting or MEG (Figure S6, Supporting Information).[29–31] It should further be noted that many other hygroscopic salts
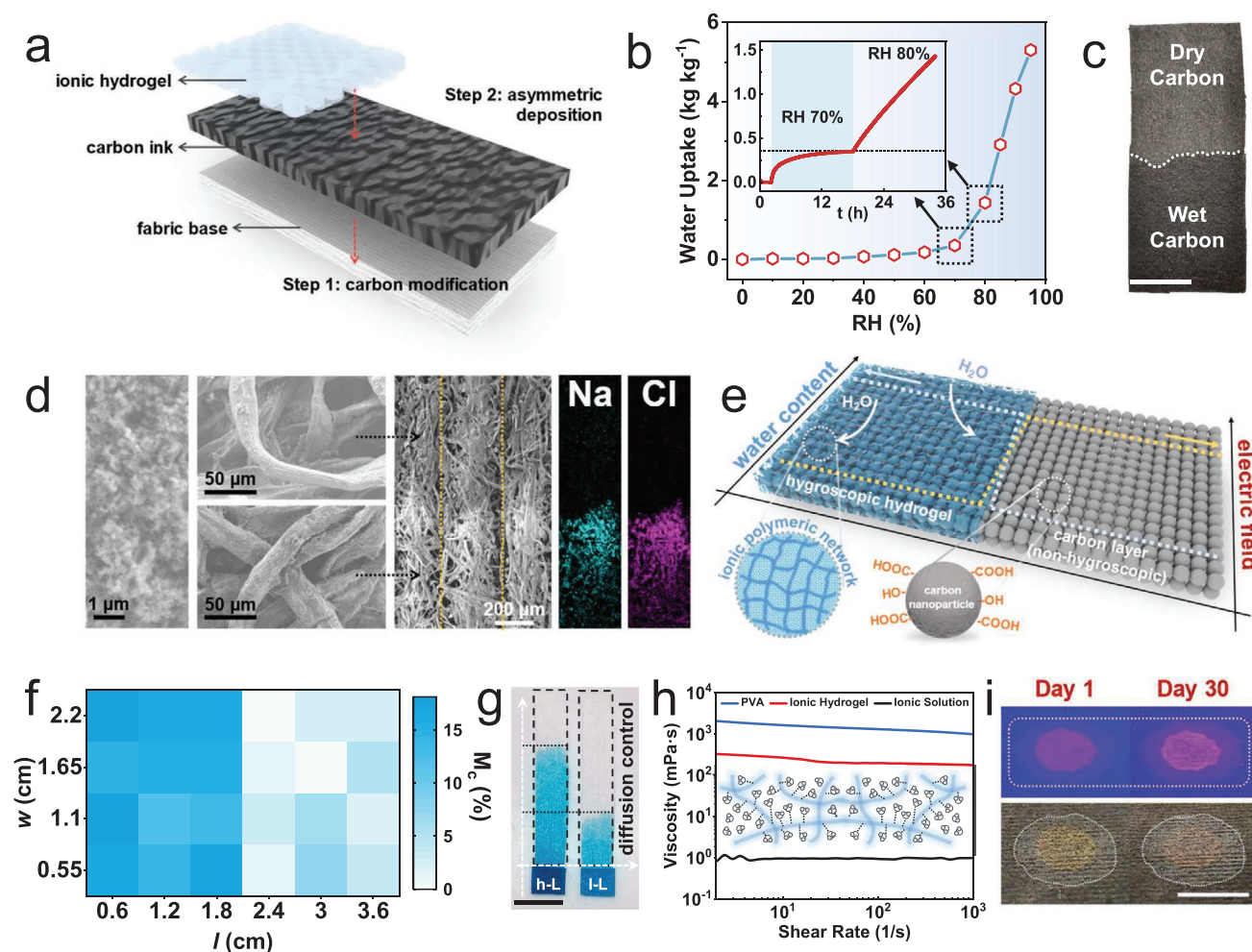
Figure 1. a) 3D schematic of the structure and fabrication process of the AHS. b) Water-absorption isotherm of ionic salt compound at 25 °C and the inset is the specific plot under RH 70% and RH 80%, indicating a sharp increase in water uptake when the RH is >70%. c) Image of the as-prepared AHS. Scale bar: 1 cm. d) SEM images and EDX element analysis maps of AHS showing the carbon nanoparticles and asymmetric structure with two clearly divided regions. e) Schematic illustration of the basic scheme of employing the AHS to reveal insights into moisture-material interactions for MEG and energy storage. f) Water mass content (denoted as Mc) map of the AHS after water absorption showing the clear water gradient across AHS. l refers to the length of the AHS and w is the width. g) Water diffusion control by leveraging the loading of ionic compound. It was demonstrated that the diffusion distance of high loading (h-L) sample was longer than that of low-loading (l-L) sample due to more water absorption. Scale bar: 1 cm. h) Viscosity measurements of pure ionic solution, ionic hydrogel, and pure PVA. The inset illustrates that water molecules are confined within the polymeric PVA network, thus inhibiting water diffusion. i) Fluorescent images under UV light (upper row) and digital pictures (lower row) of rhodamine B doped hygroscopic pattern on a carbon coated fabric. The sample was completely dried out on Day 1, and then left for water absorption for 30 days, showing no significant expansion of the wet pattern as indicated by the white dash line. Scale bar: 1 cm.

(e.g., LiCl and CaCl$_2$) fit our AHS well to probe moisture-material interactions.

The water absorption kinetics of the ionic hydrogel were significantly enhanced by the fibrous substrate (Figure S7, Supporting Information).[14] By moisture fixation, the AHS was distinctly divided into two regions, forming a tangible water gradient (Figure 1c). Water was confined within the hydrogel-covered area; thus, this wet-carbon region tended to be darker in appearance.[32] Further characterizations by scanning electron microscopy (SEM) and energy-dispersive X-ray spectroscopy (EDX) mapping also identified this sharp contrast in terms of structure and element distribution, respectively (Figure 1d). Details of the as-formed water gradient across the AHS and its correlation to the induced electric field are summarized in the

schematic in Figure 1e. Specifically, the absorbed water dramatically modified the surface state of the hydrogel-covered carbon region by spontaneously developing an EDL at the water-carbon interface. This is a spontaneous process, as the negative zeta potential of carbon black nanoparticles can readily drive the absorption of dissociated cations son their surfaces. The change in surface state generates the potential difference (i.e., electric field) across the AHS. We emphasize that keeping the dry carbon end moisture-free is essential, and of particular note is that full water infiltration from one end to the other could ultimately prevent electricity generation (Figure S8, Supporting Information).

Water distribution was mapped to further characterize the water gradient across the AHS (Figure 1f). This gradient could

be maintained in an open humid environment, despite saturated water absorption. Thus, undesirable water diffusion and infiltration could be avoided.[33] This is mainly attributed to the two practical solutions that were adopted for AHS preparation: i) careful control of the hygroscopic loading in the ionic hydrogel, and ii) construction of a hydro-polymeric network to impede water movement. To verify the efficacy of these two strategies, a series of validation tests were performed. The amount of absorbed water plays a key role and can be readily manipulated by controlling hygroscopic loading. A small amount of water slows down water diffusion and consequently determines the short diffusion distance, as shown in Figure 1g and Figure S9, Supporting Information. Confining water to a polymeric network using polymer additives was found to be more effective than controlling hygroscopic loading.[34] Quantitative evidence shows that the viscosity of the ionic hydrogel was dramatically enhanced compared to that of the pure salt solution (Figure 1h), which offers substantial resistance to the inhibition of interior water movement (Movie S1, Supporting Information). This is because the absorbed water is trapped in the hydrogel due to the formation of hydrogen bonds between the water molecules and the polymeric chains, and the bonded water no longer becomes free, despite external capillary attraction (Figure S10, Supporting Information). By coupling both strategies, the ionic hydrogel was dyed blue and deposited on a pristine fabric to monitor the water diffusion behavior throughout continuous water absorption. After a slight forward shift of the blue area due to the initial water absorption, further movement became negligible, implying that water diffusion had ceased (Figure S11, Supporting Information). This was also observed for the carbon-coated fabric. For improved visualization, rhodamine B was added to the hydrogel precursor before deposition.[35] Under UV light, the fluorescent hydrogel was confined to a small area. In contrast, the purely ionic solution diffused freely (Movie S2, Supporting Information). It was then dried and left in an open humid environment (RH of ≈80%) for water absorption. After 30 days, the fluorescent pattern showed no expansion while retaining water (Figure 1i), suggesting the feasibility of these strategies to form a permanently maintained water gradient.

2.2. Asymmetry-Induced Electricity Generation of AHS

According to our observations, during water absorption, opposite surface states (wet and dry) at the two ends of the AHS give rise to the development of an in-plane electric field, which serves as the origin of the observed voltage and current output (Figure S12, Supporting Information). Furthermore, the wet moiety acts as a negative pole, whereas the dry is always positive.[7,16,36] Prior to the discussion of the underlying mechanisms of AHS, the electric behavior was systematically outlined. Firstly, homogeneous carbon exhibited ohmic behavior; by contrast, AHS exhibited typical characteristics of an energy generator by yielding an open circuit voltage (V_{oc}) of ≈0.65 V and a short circuit current (I_{sc}) of several microamperes (**Figure 2**a). These observations were further validated by control experiments using inert electrodes (Figure S13, Supporting Information). As shown in Figure 2b, the electric output of the AHS requires that one electrode must be connected to the wet region and the other to the dry region. It is worth noting that connections within the same region lead to no response, meaning that the water-content gradient is crucial for the output. It was meanwhile observed that the generated voltage was independent of the measuring distance; however, the I_{sc} decreased as the distance increased, which was simply caused by the increasing internal resistance (Figure S14, Supporting Information). This provides useful insights into possible output improvement achieved by reducing the superfluous area and optimizing connections with minimized resistance. In contrast to previously reported MEG devices, which mostly require specific environmental conditions and can only deliver a transient electric response,[19,37] the developed AHS was able to maintain its electric performance in ambient environment owing to its permanent wet-dry asymmetry. As demonstrated in Figure 2c, the V_{oc} of AHS was stably sustained in the range 0.6–0.7 V over 150 h under constant temperature and humidity. Furthermore, it should be highlighted that the entire AHS was exposed to an open humid environment during the long-term measurements, verifying that the AHS can function during and even after full water absorption (Figure 2d).[16,18] Leaving the AHS in a humid environment over many days was found to have no effect on its performance owing to the well-defined asymmetry and strongly inhibited water diffusion (Figure S15, Supporting Information), which resulted in power generation at our disposal by the AHS. In addition to energy generation, this enduringly maintained electrical potential could be potentially useful for many other applications, especially in the field of sensing and information technology, such as multi-responsive sensors, memristor and electrochemical transformations.[25,38]

In essence, the absorbed water content determines the gradient, and hence the behavior of the AHS. It is then inferred that losing water due to an external thermal stimulus could lead to output loss, but it has been demonstrated that the functionality of the AHS is restorable after water re-absorption. A particular case of interest is the response of an AHS to sunlight. To investigate this, simulated one-sun solar radiation (1 kW m^{-2}) was employed to illuminate the AHS surface, and the V_{oc} was monitored accordingly. Under light exposure, the V_{oc} dropped dramatically, and started to rebound after the light was turned off (Figure 2e). This was attributed to the solar-thermal effect of the AHS as carbon black is a high-performance photothermal material.[39] Solar illumination effectively increased the temperature of the AHS to ≈60 °C (Figure 2f), and the localized heat caused water desorption and consequently erased the gradient.[40] It was then rebuilt when low-light conditions allowed the AHS to reabsorb moisture, leading to a rebound of V_{oc}. This conclusion was further supported by the asynchronous temperature changes in the two regions observed during the heating and cooling processes (Figure S16, Supporting Information), which stems from endothermic water desorption and exothermic water absorption, respectively. The results also indicate that, AHS demonstrates hydrolytic and structural stability with excellent reusability, as suggested by continuous cycling tests (Figure S17, Supporting Information). It is also worth noting that this reversible photothermal response of the AHS would be highly advantageous to the sunlight-powered regeneration of it for repeated use. Although sunlight illumination cannot
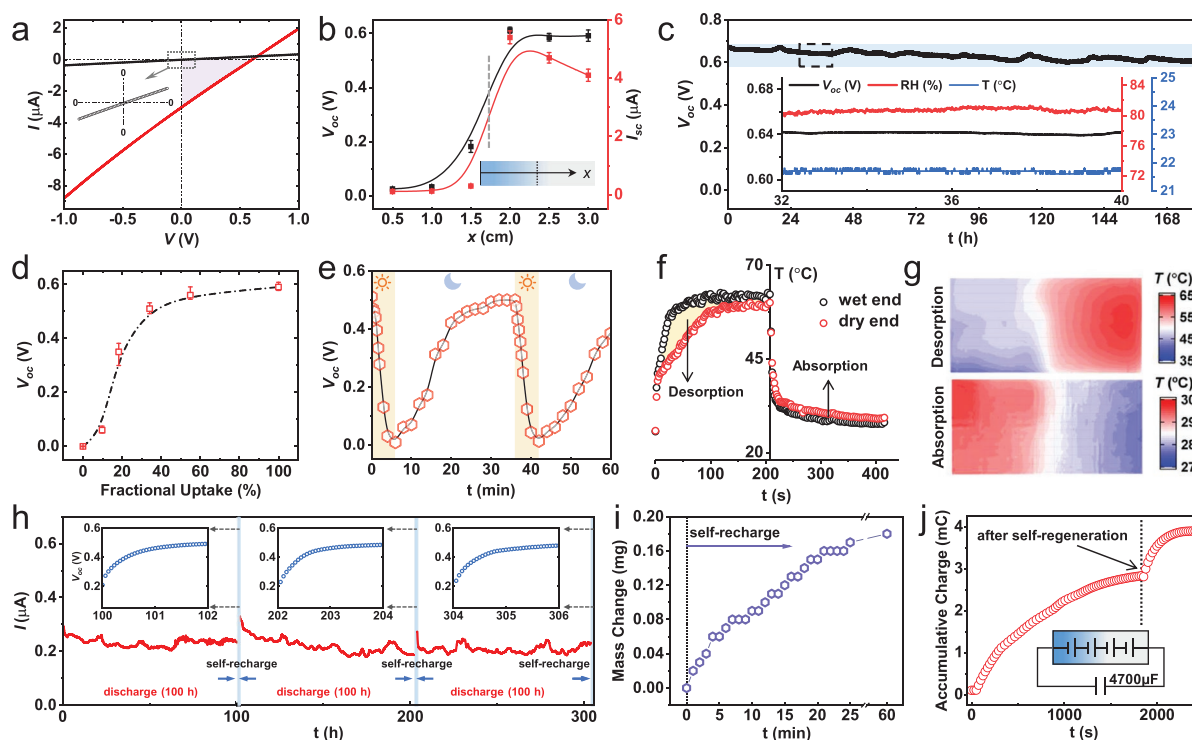
**ADVANCED
SCIENCE NEWS**
www.advancedsciencenews.com

**ADVANCED
MATERIALS**
www.advmat.de

Figure 2. a) I–V curves of pure carbon layer (black line) and the AHS (red line). b) The correlation between V_{oc}, I_{sc} and the measuring distance (x) between wet-carbon and dry-carbon. c) Continuous V_{oc} measurement under constant ambient conditions. The inset plot gives the specific records of V_{oc}, temperature and RH over a selected time range (32–40 h). d) V_{oc} as a function of the fractional water uptake of the deposited hygroscopic ionic hydrogel. e) Electric output of the AHS in response to solar irradiation. The AHS is electrically regenerated after water re-absorption. f) Temperature profiles of the wet-carbon and the dry-carbon of the AHS during solar desorption test and the following re-absorption. Light was turned off at 200 s. g) The temperature maps of the AHS under light (upper row) and dark (lower row). The differences between the two regions stems from the endo-thermic desorption process and the exothermic water absorption, respectively. h) Three long discharge/self-recharge cycles. AHS was connected with an external resistor (2.2 MΩ) for electricity discharging for 100 h, during which the output current was monitored; the external resistor was then disconnected for 2 h, leaving the AHS in open-circuit state, and V_{oc} was recorded accordingly. i) Mass change of the AHS during the self-recharging process. j) Accumulative charge stored in a capacitor (4700 µF) by connecting with 4 AHSs showing successive electricity output of AHS owing to the self-regeneration effect.

directly charge the AHS, it provides an indirect approach to enable the device to recover its energy after discharge readily by cyclic absorption/desorption.

The output duration of the AHS highly depends on the discharge current, which is further decided by its external load (Figure S18, Supporting Information). A drop in its voltage was observed after discharge, and it was interestingly found that the AHS could recharge itself, as shown in Figure 2h. The AHS could spontaneously and repeatedly recover its energy in ambient environment after it disconnected with external load (Figure S19, Supporting Information), which was a phenomenon that exhibited close similarity to the recent protein-based MEG device.[16] Further experimental observations suggested that this self-recharge capability very likely originated from the dynamic water exchange between the AHS and its surrounding moisture during discharge/self-recharge cycles (Figure S20, Supporting Information). It is because mass change was observed during the processes of discharge and self-recharge, which was marginal but might play a key role in driving the self-regeneration of the AHS (Figure 2i). It should also be noted that the exact nature of this process is still challenging to disentangle at present, which would require future explorations with spectroscopic and high-resolution surface techniques. With the

self-regeneration property, the AHS is then able to be employed for electricity accumulation by continuously harvest energy from environmental humidity (Figure 2j).

2.3. Geometry Optimization for Enhanced AHS Output

The preliminary observation was that a greater AHS size was able to increase the output with ease by amplifying I_{sc} (Figure S21, Supporting Information). Probing this further, it was shown that the final power output of an AHS is governed by the wet–dry interfacial scale, rather than the total surface area. Three AHS samples with different areas and identical widths and thickness were prepared to ensure a same-scale interface, as shown in **Figure 3**a. Power density (P) was estimated as

$$P = (V_{oc} \cdot I_{sc}) / 4 (A \cdot d) \tag{1}$$

where A is the projected area, as illustrated in Figure S22, Supporting Information, and d is the thickness ($\approx$0.3 mm). Notably, the smallest A_1 delivered the highest power density (Figure 3b), which was $\approx$70 µW cm^{-3}, corresponding to $\approx$226 µW g^{-1} based on the overall density of the AHS ($\approx$0.31 g cm^{-3}). It should be

**ADVANCED
SCIENCE NEWS**

www.advancedsciencenews.com
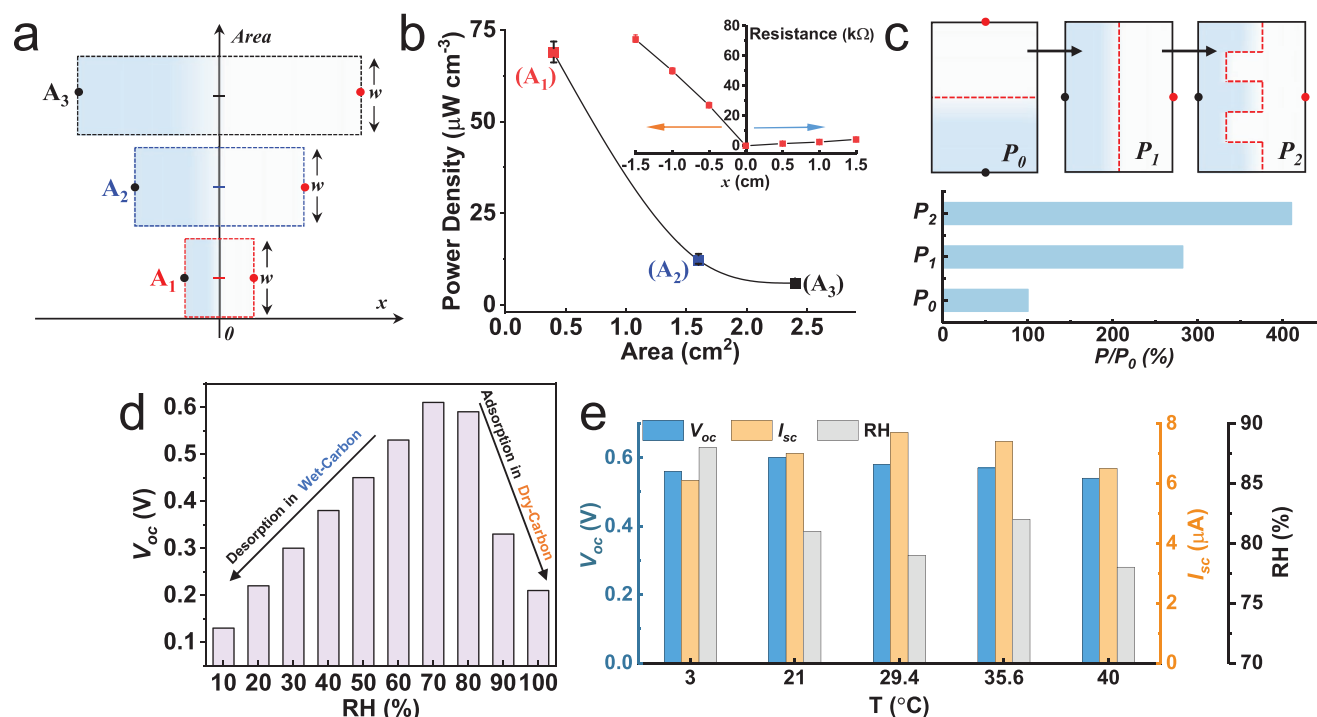
**ADVANCED
MATERIALS**

www.advmat.de

Figure 3. a) Illustrations showing three asymmetric configurations of AHSs with the same width (w) but different length, thus different area, which are denoted as A_1, A_2, and A_3, respectively. The black and red dots signified the positions of two electrodes for measurements. b) Calculated power density of the three AHSs as a function of their area. The inset shows the resistance measured starting from the origin point towards the wet region (orange arrow) and dry region (blue arrow). c) Optimized geometry of the AHS to maximize power density. Three geometries were devised and their power outputs are denoted as P_0, P_1, and P_2, respectively. The wet–dry contact interface is highlighted by red dash line. d) Electric performance of AHS in response to varying RH. e) AHS performance as a function of temperature that was measured within the RH range of 70–90%.

noted that the estimation was performed in the volumetric unit, as increasing its thickness could also scale up the output, which can be readily realized by stacking multilayer AHS. This exceptional enhancement achieved by A_1 in comparison with A_2 and A_3 originates from the following two synergetic contributions: i) the significantly reduced area in calculation, and ii) the dramatic increase in I_{sc} due to reduced internal resistance (the inset in Figure 3b). Compared to its MEG predecessors, tangible improvement has been made, as evidenced by the reported performance of the AHS (Table S1, Supporting Information). The findings also suggest that, further improvement would require enhanced conductivity in both the base carbon layer and the hygroscopic hydrogel.[41] In addition, the surface morphology of the substrate material for AHS significantly impacts its conductivity at a given carbon loading (Figure S23, Supporting Information). Thus, creating as many wet-dry contact interfaces as possible within a given carbon area should maximize output. With reference to these conclusions, three different geometries were devised by using same-sized AHSs with the same amount of hydrogel, but with unequal interface lengths (Figure 3c). As more interfaces were involved, a considerable improvement was successfully realized, and P_2, with the maximum interface, exhibited an output of four times that of the original P_0.

As a moisture-triggered energy generator whose energy source is humidity, the performance of an AHS inevitably depends on environmental humidity. This influence works in a similar way to thermal desorption in adjusting the gradient by

leveraging the absorbed water content. The results obtained by testing the AHS under different RHs show that the optimum humidity is found between 70% and 90%, and this is also the range where the water absorption by sea salt begins to rise (Figure 3d). Either decreasing or increasing the RH could lead to a drop in performance, which is explained by water desorption in the wet region and enhanced water condensation in the dry region (Figure S24, Supporting Information). To widen this range, the step presented in the isotherm profile of the ionic compound was expected to shift to the left, that is, further regulation is required to ensure that water absorption occur at lower RH. Another feasible method is to employ other hygroscopic salts of lower deliquescent RH (DRH) than sea salt compounds (Figure S25, Supporting Information),[42] such as LiCl, whose DRH is only ≈11%. This is mainly because the excellent compatibility of AHS with various hygroscopic salt species. It is worth noting that, if the RH could be maintained in a recommended range, the AHS could work across a wide temperature range (Figure 3e and Figure S26, Supporting Information). It is because hygroscopic salts are still able to absorb water from the air as long as the RH requirement is satisfied, despite the environmental temperature and the air vapor density.[43] The temperature effect is magnified when the RH changes with temperature by adjusting the water gradient (Figure S27, Supporting Information). For example, at an air vapor density of 10 g kg^{-1}, increasing the temperature from 16 to 33 °C would decrease the local RH from 90% to 30%, which might easily give rise to water desorption of the AHS. This case would be

**ADVANCED
SCIENCE NEWS**

www.advancedsciencenews.com

**ADVANCED
MATERIALS**

www.advmat.de

very similar to the photothermal desorption of the AHS under natural sunlight. In addition, previous studies suggest that increasing the temperature could improve the surface charge density at water-materials interfaces and the capacitance.[44,45] Hence, an increase in temperature at recommended RH is believed to enhance the performance of AHSs.

2.4. Working Principle of the AHS

Based on the above observations, we summarize here that an in-plane potential difference is established across the AHS owing to selective water absorption and the resulting wet–dry asymmetry. The AHS functions optimally following saturated water absorption rather than during the process of water absorption (**Figure 4**a and Figure S28, Supporting Information). Thus, the AHS shows a distinct working mechanism that drives electricity generation in a static manner without the restriction of water uptake saturation, making it distinct from

most prior MEG devices. It also behaves differently from other energy generators that extract electricity from mechanical flow, such as electrokinetic generators, which rely heavily on gravity in a specific vertical configuration to sustain continuous water flow for electricity generation.[46] We attribute this to a hygro-ionic effect because the hygroscopicity of the saline hydrogel and the subsequent ionic interaction with carbon account for these findings.

We first employed a Kelvin probe force microscope (KPFM) to perform a potential scan over the carbon surface before and after it was slightly moisturized. The obtained KPFM images (Figure 4b) clearly suggest that water absorption decreases the surface potential, thus making the dry moiety of the AHS the anode. This result is consistent with our experimental observations, implying that the in-plane electric field originates from the reduction in the surface potential of the wet moiety only. The KPFM results also agrees well with previous reports,[36] where an excess of negative charge carriers produced by the water-absorbing surface drives the output voltage. An average
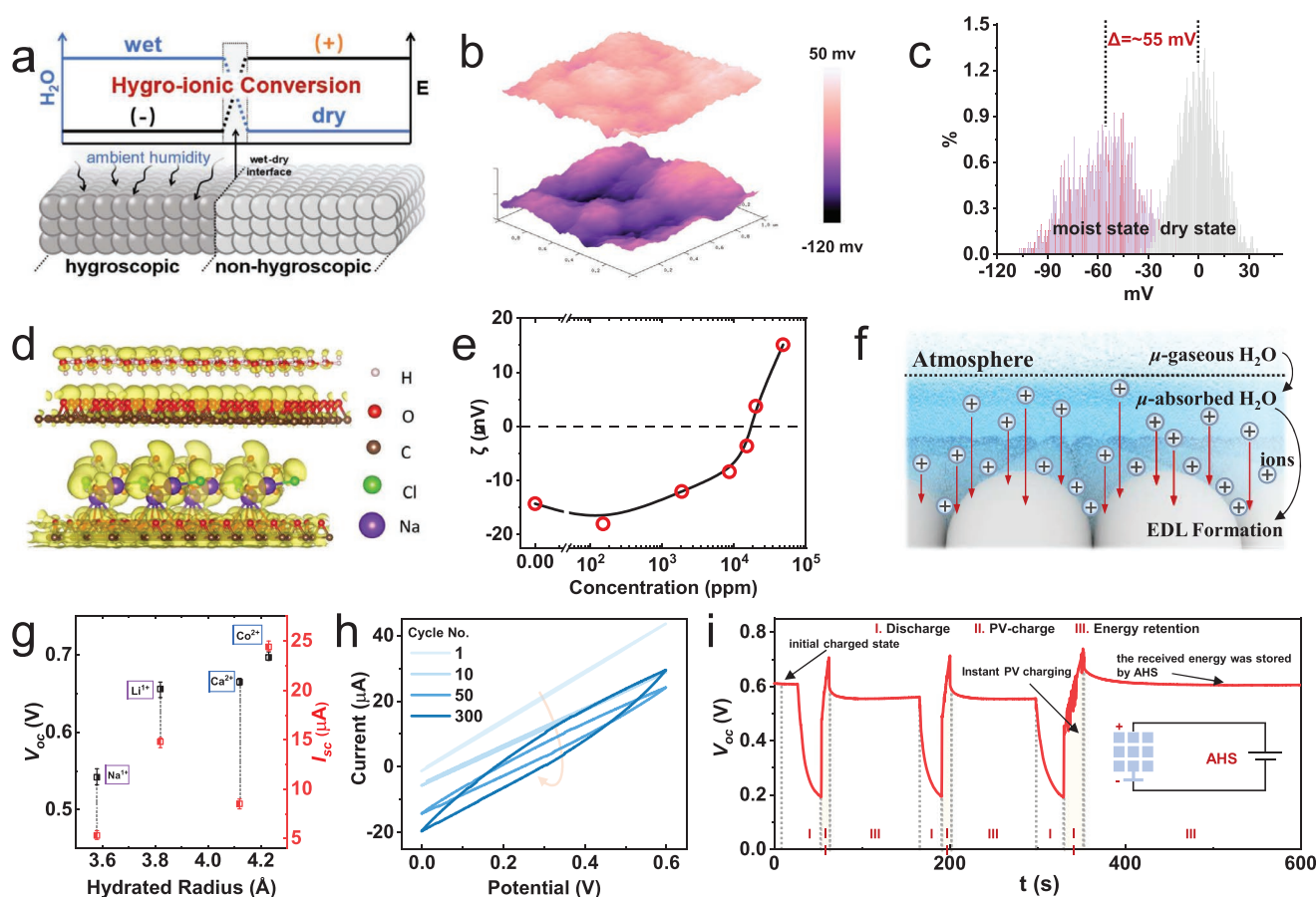

Figure 4. a) Schematic illustrating the basic observations obtained from the AHS after water absorption. b) KPFM images of carbon surface before (top panel) and after (bottom panel) slight water absorption. c) Surface potential distributions of KPFM results. d) Surface charge accumulations by using water (top panel) and ionic solution (bottom panel) on oxidized graphene. NaCl embedded water solution was employed as ionic solution to simplify the simulation with ionic solution. The isosurface density is in the unit of 0.003 eV Å^{-3}. e) Zeta (ζ) potential of carbon black as a function of ionic concentration. f) Schematic illustrating the energy conversion pathways within AHS system based on cation adsorption to carbon surface for EDL formation. μ refers to the chemical potential of water in gaseous and absorbed state. g) Electric behavior in response to different hydrated radius and valence state of hygroscopic ionic compound. h) Operando CV curves of the AHS measured in the process of water absorption. Scan rate: 50 mV s^{-1}. i) Charging a discharged AHS by PV panel. Energy received from PV was successfully retained, showing the potential of AHS for application as an energy storage device.

**ADVANCED
SCIENCE NEWS**

www.advancedsciencenews.com

**ADVANCED
MATERIALS**

www.advmat.de

potential drop only 55 mV was measured because the water content was strictly controlled at a low level during the measurement (Figure 4c). To understand the roles of the water and ions in this process, density functional theory (DFT) simulations were performed, in which Bader charge transfer of ionic water on the oxidized graphene surface was calculated (Figure 4d). Although the carbon black structure is not entirely graphitic, oxygen-functionalized graphene has been widely accepted for DFT investigations of water-material interactions.[5] It was shown that charges are induced and accumulated on the graphene layer when it meets water (0.0031e from one H_2O molecule). In contrast, by covering the oxidized graphene with saline water (represented by NaCl-embedded water), 0.0189e is transferred from every water molecule, nearly six times that from pure water. The presence of ions significantly increases the surface charge density thereby enhancing the hygro-interaction, and thus, offering a critical contribution to the generation of electricity.

The reduced surface energy and adsorbed Na^+, as illustrated by the DFT simulation, imply that an EDL is formed over the carbon layer. In addition, the carbon black employed here as a stage for the asymmetric structure is a well-known material that can naturally develop an EDL by adsorbing cations when in contact with aqueous solution.[7] Experimental evidence of cation adsorption by the EDL on carbon black is the observed inversion of its zeta (ζ) potential from originally negative to positive with increasing ionic concentration (Figure 4e).[47] This explains, why the water content is critical for realizing the optimal V_{oc}. According to the Stern model,[48] the developed potential difference depends on the surface charge density of the EDL (see details in the Supporting Information), which is determined by the number of adsorbed cations. More cations can be produced with increasing water absorption, and at the same time, the EDL gradually forms by covering more carbon black particles. Oxygen-containing functional groups (e.g., carboxyl) play a key role in enhancing charge-transfer interactions with water and donating protons for EDL adsorption. To confirm the contribution from the oxygen-containing functional groups, AHS devices prepared by pristine carbon nanotubes (CNT) and oxidized CNT (O-CNT) were compared. The results show that the O-CNT-based AHS exhibited much improved electric performance than the pristine CNT (Figure S29, Supporting Information). The adsorption process also explains why the measured V_{oc} was larger when the AHS was in standby, as the surface charge accumulates over time. Thus, the energy flow involved in the AHS was elucidated. As all the electrical signals were observed only after water absorption, it was concluded that ambient humidity served as the sole energy source. The phase change of water from the gaseous state to the absorbed state initiates the subsequent ionic dissociation. The generated cations are then adsorbed onto the carbon surface for EDL formation, which simultaneously stores energy (Figure 4f). Although the EDL covers the entire wet region, only the cations aggregated at the contact interface of the two electrodes (i.e., the wet-dry interface) are involved in the final current generation, which is analogous to the equivalent process in capacitors.

The proposed EDL model was further validated using cations of different ionic radii and valence states (Figure 4g). Four widely used desiccant chlorides—LiCl, NaCl, $CoCl_2$, and $CaCl_2$ were selected at identical molar concentrations. The known relationship suggests that the potential drop across the Stern layer of the EDL is positively correlated with its thickness.[48] Thus, the V_{oc} was enhanced as the radius of the hydrated ions increased owing to the resulting increase in layer thickness (see details in Supporting Information). Notably, Co^{2+} exhibited the highest V_{oc} and I_{sc} owing to the synergy of its large radius and divalent nature. The results also imply that by replacing the selected NaCl-rich ionic compound with other hygroscopic agents, such as LiCl and $CoCl_2$, the power density of the AHS can be greatly multiplied by several times. This did not change our conclusions obtained with the sea salt compound.

To further confirm the capacitive behaviors induced by the EDL, operando cyclic voltammetry (CV) tests (scan rate: $50 \, mV \, s^{-1}$) were performed on a fully desorbed AHS based on a two-electrode configuration. Notably, as the cycle number increased, the curve began to show an expanded area owing to water absorption over time (Figure 4h). In contrast, the CV curve of a water-absorbed AHS immediately exhibited such area, which confirmed the major contribution from the absorbed water (Figure S30, Supporting Information). The typical capacitor-shaped curve also suggests that no redox reactions are involved in the system. As such, the capacitance generated after water absorption lays the groundwork for energy generation and storage by AHS. This enables the AHS to behave like a capacitor, and theoretically, it is possible to charge its EDL again via external electrical means for energy storage, which has been confirmed experimentally. Specifically, as shown in Figure 4i and Figure S31, Supporting Information, after discharge (Stage I), the AHS was immediately connected to a photovoltaic (PV) panel, and its voltage increased substantially in seconds (Stage II). The received energy was then successfully retained by the AHS as indicated by the maintained V_{oc} after disconnection (Stage III). Cyclic measurements were further performed, which indicated that the capacity of energy storage by AHS depends on the charging time and voltage (Figure S32, Supporting Information). This demonstration could serve as interesting evidence to eminently distinguish AHSs from other moisture-driven generators, as an MEG device could also be applied for active energy storage.[24] Interestingly, it was further demonstrated in Figure S33, Supporting Information that the AHS could also be charged to recover its energy by a triboelectric nanogenerator (TENG), which opens up new possibilities of charging AHS by mechanical energy harvested from the surrounding environment.

2.5. AHS-Assembled Device

AHSs hold promise as a proven technology for immediate application owing to their excellent compatibility with various substrate materials and exceptional ease of scalability. The fabric employed here is commercially available, and thus the fabric-based AHS is highly scalable for mass production (**Figure 5**a), at a cost of only ≈$0.15 per m^2 (Figure S34, Supporting Information). It is also noteworthy that the total fabrication process of AHS from raw materials to finished products can be completed within 15 min (Movie S3, Supporting Information).
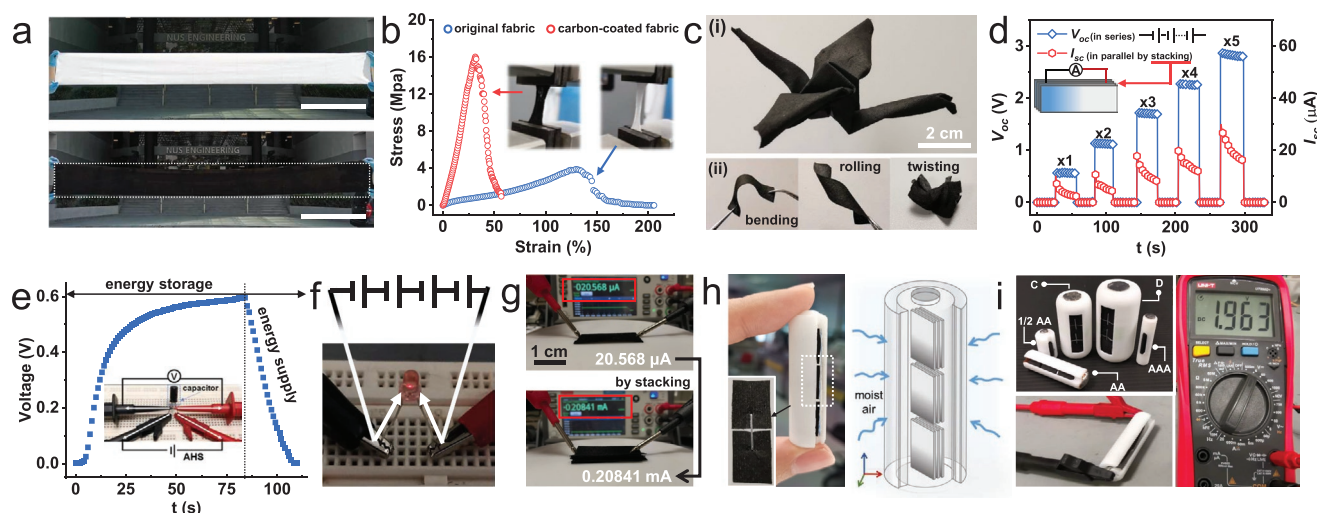
**ADVANCED
SCIENCE NEWS**

www.advancedsciencenews.com

**ADVANCED
MATERIALS**

www.advmat.de

Figure 5. a) Large-scale fabrication of the fabric-based AHS showing its excellent scalability. Scale bar: 0.5 m. b) Tensile strength of the pristine fabric and the as-prepared carbon coated fabric, indicating enhanced mechanical strength after carbon modification. c) Flexibility of the fabric-based AHS. It is then possible to fold an origami crane with a large-size carbon coated fabric (i), and the carbon coated fabric can be easily bent, rolled, and twisted (ii). d) Scaled-up V_{oc} and I_{sc} by connecting multiple AHSs in series and in parallel. Particularly, the parallel connection was performed via simple stacking. e) Electricity storage in capacitor. A single AHS was connected to a capacitor (47 μF), and the capacitor was quickly charged up to a voltage similar to the V_{oc} of AHS. f) Direct electricity output demonstrated by lighting up an LED with four AHSs. g) Stacking multiple AHSs toward mA-scale output. h) Photos and schematics of an AHS-assembled AA-sized power device. Multiple stacks of AHSs were connected by staples and embedded in a 3D printed battery case. i) Electricity generation of the AHS-assembled device. The size of the device is same as traditional AA battery, and its V_{oc} reaches up to 1.96 V.

Furthermore, the as-fabricated AHS was mechanically robust for practical applications. As shown in Figure 5b, the carbon coating significantly reinforced the pristine fabric by increasing its tensile strength from 4 to 16 MPa. Although the strength of the fabric is not particularly high, it is comparable to that of synthetic fabrics such as those fabricated via electrospinning.[49] We further show that even the original fabric is sufficiently strong to meet the mechanical demands of various application scenarios of AHSs (Figure S35, Supporting Information). The AHS also exhibits outstanding flexibility (Figure 5c), as demonstrated by the folding of an origami crane using a large piece of AHS fabric (Movie S4, Supporting Information). Bending, rolling, and twisting the AHS had no impact on its electric performance (Figure S36, Supporting Information).

Scaling up the power output of the AHS is necessary and can be readily achieved by connecting multiple devices in series and parallel, which can enhance V_{oc} and I_{sc} (Figure 5d), respectively. In particular, the parallel configuration can be alternatively performed by stacking AHSs, such that the connection is considerably simplified (Figure S37, Supporting Information). There are three modes of power output from the AHS. Storing the generated electricity in a capacitor is an effective way to make it more accessible when required (Figure 5e). An AHS can also be used directly for energy supply. Four newly prepared AHSs were connected in series and naturally charged after water absorption (Figure S38, Supporting Information). They were then employed to power an LED. Because the LED has a low power demand (90 μW under an input voltage of 1.5 V), the AHS is readily able to light it (Figure S39, Supporting Information). In this demonstration, the LED could be sustained by only four pieces of AHSs for up to 2 minutes (Figure 5f and Movie S5, Supporting Information).

In light of this, the current output of the AHS can readily be enhanced up to the mA level via simple stacking of multiple AHS devices without affecting the voltage (Figure 5g). Packaging AHSs into a bulk apparatus could pave the way to their implementation in common daily scenarios. To achieve this, an AA-sized battery case was prototyped and employed to accommodate the AHS sets (Figure 5h). Each set comprised three small pieces of AHS in a stack, and three AHS sets were connected in series simply via stapling (Figure S40, Supporting Information). The as-assembled device successfully demonstrated a V_{oc} as high as 1.96 V as shown in Figure 5i and Movie S7, Supporting Information. This performance is satisfactory for powering small electronic devices, such as an alarm clock (Movie S7, Supporting Information). The energy density can be further improved by fully packing the interior space with AHSs. Similarly, the AHS is highly compatible with other pen-light devices of various sizes, including C-size, D-size, AAA, and 1/2 AA (Figure S41, Supporting Information). Additionally, a coin cell of AHSs was also obtained (Figure S42, Supporting Information).

3. Conclusion

In summary, we have designed an intriguing structure with asymmetric hygroscopicity to provide insights into moisture-material interactions. The developed AHS successfully demonstrated the capacity for energy harvesting from ambient humidity, which has been repeatedly investigated as a green energy source in recent years.[50] By employing a hygroscopic ionic hydrogel, a water gradient was spontaneously formed across the AHS after asymmetric water absorption. This

**ADVANCED
SCIENCE NEWS**

www.advancedsciencenews.com

**ADVANCED
MATERIALS**

www.advmat.de

asymmetry was permanently maintained owing to the construction of a diffusion-inhibited polymeric hydro-network. We have shown that asymmetry plays a key role in realizing hygro-ionic conversion for MEG and subsequent energy storage. It durably sustains the voltage output of the AHS and allows it to be freely exposed to a humid environment, even after full water absorption. A series of characterizations and measurements were carried out to elucidate its electric behavior, as well as the hygro-ionic mechanism (Figure S43, Supporting Information). Notably, the AHS demonstrates an ultrahigh peak power density ($\approx$70 μW cm^{-3} or $\approx$226 μW g^{-1}) with rational geometry optimization. The self-regeneration of the AHS, which relies on dynamic water desorption/absorption or can be alternatively driven by natural sunlight illumination, allows it to continuously harvest energy from the ambient environment in a cyclic operation mode. Moreover, it can be recharged by an external input, such as a PV source and TENG, making the AHS the first MEG device of its kind that is capable of simultaneous energy generation and storage. This system exhibited good cyclic stability for sustainable operation. Owing to the ease of scalability of the AHS, penlight devices by comprising multiple AHSs were further highlighted as a proof-of-concept for practical implementation, which would enable the broad application of AHS for daily use. With a distinctive energy conversion route, we believe that AHSs offer informative insights toward a deeper understanding of moisture–material interactions.

4. Experimental Section

Fabrication of the Asymmetric Hygroscopic Structure: The functionalized carbon ink was prepared by mixing carbon black (100% compressed, Alfa Aesar) and sodium dodecyl benzene sulfonate (SDBS, Sigma Aldrich) at a weight ratio of 1:1. Typically, 1 g of the mixture was dispersed into 100 mL deionized (DI) water via ultrasonication. The obtained carbon ink was then employed for surface carbon layer formation over a commercially available non-woven fabric (thickness: $\approx$0.3 mm, Shanghai Kangji Co. Ltd.) by dip coating. The fabric is made of wood pulp (weight percentage: 55%) and polyester (weight percentage: 45%) at an overall density of $\approx$0.00625 g cm^{-2}, and its fiber has a width of $\approx$25 μm. This coating process was repeated for several times until the fabric was uniformly covered by a black carbon coating. The authors employed artificial sea salt (ASTM D1141-98, Lake Products Company LLC) as the ionic compound for the fabrication of the hygroscopic ionic hydrogel. Salt solution was first prepared and then mixed with polyvinyl alcohol (PVA, Sigma Aldrich) solution. Specifically, PVA powders was fully dissolved in DI water at 90 °C, forming a transparent aqueous solution (4 wt%). Ionic solution and the PVA solution were then mixed. The weight percentages of salt compound and PVA were 5% and 3% in the final mixed aqueous solution, respectively. Note that increasing the ionic concentration may result in the formation of solid crosslinking floc. The obtained ionic hydrogel precursor solution was then dropped onto one end of the carbon coated fabric. To permanently confine water within a limited region and avoid capillary infiltration through the fabric, the amount of ionic hydrogel to deposit onto carbon surface was carefully controlled, which is highly dependent on the size of AHS to fabricate and the times of repetition of hydrogel deposition process. The hydrogel decorated carbon coated fabric was then dried out at 70 °C, and then started water absorption at ambient conditions ($\approx$RH 80%, 21 °C) as a newly prepared AHS.

Preparation of Oxidized Carbon Nanotubes (O-CNT): Water dispersion of 1 wt% multi-walled carbon nanotubes (MWCNT, purity>95%, diameter: 30–50 nm, length: 10–20 μm) was purchased from Nanostructured and Amorphous Materials, Inc. To prepare O-CNT,

20 mL of the CNT dispersion was added to 60 mL of 70% nitric acid, and the mixture solution was heated at 70 °C for 6 h. The obtained O-CNT was collected via vacuum filtration, and then rinsed by DI water until the final dispersion had a neutral pH.

Characterizations and Measurements: The natural deliquescence of ionic salt compound at ambient conditions was monitored by an optical microscope (Nikon Eclipse LV1000 and Digital Sight DS-U1). The quantified water absorption capability at various RH, namely the water absorption/desorption isotherm, was identified by a dynamic vapor sorption analyzer (Aquadyne DVS) at a constant temperature of 25 °C. Note that the ionic sample for the isotherm measurement was grinded into fine particles in advance. Other water uptake measurements via the net mass changes of ionic compound, PVA and AHS were all performed by an electronic balance (Sartorius CP224S). The water content map of AHS was also obtained in a similar way by comparing the mass change before and after water absorption. Specifically, a large-size AHS sheet was first prepared in dehydration state, and it was then cut into small pieces. The weight of each small piece was accurately recorded. After water absorption, the mass change, that is, the water content, of each small piece was readily extracted. By gathering this information from all the small pieces, the water distribution map of the original AHS was accordingly obtained. The microstructures and element distribution of AHS were characterized collectively by SEM (Zeiss Supra 40VP). The chemical composition of the prepared carbon coated fabric that was measured by Fourier-transform infrared spectroscopy (FTIR) and X-ray photoelectron spectroscopy (XPS) were respectively conducted by Agilent Cary 660 spectrometer and Kratos Axis Ultra DLD spectrometer. A UV–vis–NIR spectrometer (Agilent Cary 5000) was employed for transparency measurements of the prepared samples on glass slides. Viscosity measurements were conducted by an automatic rheometer (MCR302, Anton Paar). Rhodamine b (Sigma Aldrich) was employed to mix with ionic precursor solution aforehand to form fluorescent pattern on carbon coated fabric, such that possible expansion of the wet region caused by water diffusion could be clearly observed under UV light. Kelvin probe force microscope (KPFM) measurements were performed using Dimension Icon (Bruker Nano Surfaces). Samples for KPFM scanning were prepared at dry state and moisturized state (Mc $\approx$ 5%) by slightly doping of ionic compound. Zeta potential of carbon nanoparticles was measured by NanoBrook ZetaPALS (Brookhaven). A solar simulator (Newport 92250A-100) was employed to simulate one-sun light illumination (1 kW m^{-2}, AM1.5) for tests of AHS in response to solar light. The temperature maps of AHS under light and dark conditions were both extracted from IR images by using an IR camera (FLIR One Pro). A semi-micro analytical balance (Shimadzu AP125WD) was employed to monitor the mass changes of the AHS during discharging and recharging process. The mechanical strength of pristine fabric and carbon coated fabric were measured by an Instron 4505 tensile machine. The cyclic voltammetry (CV) measurements were obtained via an electrochemical workstation (CHI660E, CH Instruments, Inc.) All the other electrical measurements involved in this study including the four-probe measurements was carried out by Keithley 2400 and 2450 (Tektronix). Temperature and humidity were monitored by Kestrel 5000 Environmental Meter. For measurements under various RH, AHS was enclosed in a small closed cabinet where the inside RH was regulated via adjusted ventilation with wet or dry carrier air. Two capacitors (4700 μF, 25 V, WKXC; 47 μF, 16 V, Jackcon Capacitor Electronics Co., Ltd.) and an LED (FR3863X, Stanley Electric Co., Ltd.) were employed for electricity supply demonstrations. The specific power demands of the LED under different voltage input are provided in Figure S39, Supporting Information. A polysilicon solar panel was used for charging AHS under ambient room light ($\approx$0.01 kW m^{-2}).

Device Assembly: The triboelectric nanogenerator (TENG) was prepared readily by attaching a tape film (3M) and a polytetrafluoroethylene (PTFE, Latech Scientific Supply Pte. Ltd.) to copper tapes, as illustrated in Figure S33, Supporting Information. Penlight device were printed via a 3D printer (Up Box plus; Tiertime) by using the filament of acrylonitrile butadiene styrene (ABS). To embed AHS into the battery prototypes in series configuration, stacks of small

**ADVANCED
SCIENCE NEWS**

www.advancedsciencenews.com

**ADVANCED
MATERIALS**

www.advmat.de

pieces of AHS were prepared, and each stack has multiple layers. It is challenging to integrate multiple AHSs in a limited space. For a successful demonstration, the authors employed a stapler to enable the connections. Specifically, the dry end of one AHS stack was stapled with the wet end of another AHS stack, and the back side of AHS stacks were stapled together with a thin plastic sheet, which would serve as a stiff substrate for robust physical installation. Note that corrosion of the staple might occur due to the contact with saline water of the wet region of AHS, and stainless connection is expected to prevent this issue. Based on this idea, embedding more AHSs made it possible to power small electronics for daily use, and an alarm clock that was purchased from Daiso Singapore Pte. Ltd. was then employed for the powering demonstration.

Supporting Information

Supporting Information is available from the Wiley Online Library or from the author.

Acknowledgements

Conflict of Interest

The authors declare no conflict of interest.

Data Availability Statement

The data that support the findings of this study are available from the corresponding author upon reasonable request.

Keywords

[1] P. A. Thiel, T. E. Madey, *Surf. Sci. Rep.* **1987**, *7*, 211.
[2] L. Zhang, Z. Xu, L. Zhao, B. Bhatia, Y. Zhong, S. Gong, E. N. Wang, *Energy Environ. Sci.* **2021**, *14*, 1771.
[3] Y.-H. Wang, S. Zheng, W.-M. Yang, R.-Y. Zhou, Q.-F. He, P. Radjenovic, J.-C. Dong, S. Li, J. Zheng, Z.-L. Yang, G. Attard, F. Pan, Z.-Q. Tian, J.-F. Li, *Nature* **2021**, *600*, 81.
[4] O. Björneholm, M. H. Hansen, A. Hodgson, L.-M. Liu, D. T. Limmer, A. Michaelides, P. Pedevilla, J. Rossmeisl, H. Shen, G. Tocci, E. Tyrode, M.-M. Walz, J. Werner, H. Bluhm, *Chem. Rev.* **2016**, *116*, 7698.
[5] G. Xue, Y. Xu, T. Ding, J. Li, J. Yin, W. Fei, Y. Cao, J. Yu, L. Yuan, L. Gong, J. Chen, S. Deng, J. Zhou, W. Guo, *Nat. Nanotechnol.* **2017**, *12*, 317.
[6] W. Xu, H. Zheng, Y. Liu, X. Zhou, C. Zhang, Y. Song, X. Deng, M. Leung, Z. Yang, R. X. Xu, Z. L. Wang, X. C. Zeng, Z. Wang, *Nature* **2020**, *578*, 392.

[7] T. G. Yun, J. Bae, A. Rothschild, I.-D. Kim, *ACS Nano* **2019**, *13*, 12703.
[8] Y. Zhang, D. K. Nandakumar, S. C. Tan, *Joule* **2020**, *4*, 2532.
[9] D. K. Nandakumar, J. V. Vaghasiya, L. Yang, Y. Zhang, S. C. Tan, *Nano Energy* **2020**, *68*, 104263.
[10] L. Yang, D. K. Nandakumar, L. Miao, L. Suresh, D. Zhang, T. Xiong, J. V. Vaghasiya, K. C. Kwon, S. C. Tan, *Joule* **2020**, *4*, 176.
[11] X. Li, B. Ma, J. Dai, C. Sui, D. Pande, R. Smith David, L. C. Brinson, P.-C. Hsu, *Sci. Adv.* **2021**, *7*, eabj7906.
[12] M. Ejeian, R. Z. Wang, *Joule* **2021**, *5*, 1678.
[13] J. Lord, A. Thomas, N. Treat, M. Forkin, R. Bain, P. Dulac, C. H. Behroozi, T. Mamutov, J. Fongheiser, N. Kobilansky, S. Washburn, C. Truesdell, C. Lee, P. H. Schmaelzle, *Nature* **2021**, *598*, 611.
[14] J. Yang, X. Zhang, H. Qu, Z. G. Yu, Y. Zhang, T. J. Eey, Y.-W. Zhang, S. C. Tan, *Adv. Mater.* **2020**, *32*, 2002936.
[15] N. Hanikel, X. Pei, S. Chheda, H. Lyu, W. Jeong, J. Sauer, L. Gagliardi, M. Yaghi Omar, *Science* **2021**, *374*, 454.
[16] X. Liu, H. Gao, J. E. Ward, X. Liu, B. Yin, T. Fu, J. Chen, D. R. Lovley, J. Yao, *Nature* **2020**, *578*, 550.
[17] H. Wang, Y. Sun, T. He, Y. Huang, H. Cheng, C. Li, D. Xie, P. Yang, Y. Zhang, L. Qu, *Nat. Nanotechnol.* **2021**, *16*, 811.
[18] T. Xu, X. Ding, Y. Huang, C. Shao, L. Song, X. Gao, Z. Zhang, L. Qu, *Energy Environ. Sci.* **2019**, *12*, 972.
[19] H. Cheng, Y. Huang, F. Zhao, C. Yang, P. Zhang, L. Jiang, G. Shi, L. Qu, *Energy Environ. Sci.* **2018**, *11*, 2839.
[20] U. Legrand, D. Klassen, S. Watson, A. Aufoujal, B. Nisol, R. Boudreault, K. E. Waters, J.-L. Meunier, P.-L. Girard-Lauriault, M. R. Wertheimer, J. R. Tavares, *Ind. Eng. Chem. Res.* **2021**, *60*, 12923.
[21] S. Zheng, J. Tang, D. Lv, M. Wang, X. Yang, C. Hou, B. Yi, G. Lu, R. Hao, M. Wang, Y. Wang, H. He, X. Yao, *Adv. Mater.* **2022**, *34*, 2106410.
[22] Y. Liang, F. Zhao, Z. Cheng, Y. Deng, Y. Xiao, H. Cheng, P. Zhang, Y. Huang, H. Shao, L. Qu, *Energy Environ. Sci.* **2018**, *11*, 1730.
[23] Y. Tao, Z. Wang, H. Xu, W. Ding, X. Zhao, Y. Lin, Y. Liu, *Nano Energy* **2020**, *71*, 104628.
[24] D. Shen, W. W. Duley, P. Peng, M. Xiao, J. Feng, L. Liu, G. Zou, Y. N. Zhou, *Adv. Mater.* **2020**, *32*, 2003722.
[25] T. Fu, X. Liu, H. Gao, J. E. Ward, X. Liu, B. Yin, Z. Wang, Y. Zhuo, D. J. F. Walker, J. Joshua Yang, J. Chen, D. R. Lovley, J. Yao, *Nat. Commun.* **2020**, *11*, 1861.
[26] C.-N. Yeh, K. Raidongia, J. Shao, Q.-H. Yang, J. Huang, *Nat. Chem.* **2015**, *7*, 166.
[27] Y. Zhang, H. Zhang, T. Xiong, H. Qu, J. J. Koh, D. K. Nandakumar, J. Wang, S. C. Tan, *Energy Environ. Sci.* **2020**, *13*, 4891.
[28] Y. Zhang, T. Xiong, D. K. Nandakumar, S. C. Tan, *Adv. Sci.* **2020**, *7*, 1903478.
[29] P. Zieger, O. Väisänen, J. C. Corbin, D. G. Partridge, S. Bastelberger, M. Mousavi-Fard, B. Rosati, M. Gysel, U. K. Krieger, C. Leck, A. Nenes, I. Riipinen, A. Virtanen, M. E. Salter, *Nat. Commun.* **2017**, *8*, 15883.
[30] Y. Xia, Q. Hou, H. Jubaer, Y. Li, Y. Kang, S. Yuan, H. Liu, M. W. Woo, L. Zhang, L. Gao, H. Wang, X. Zhang, *Energy Environ. Sci.* **2019**, *12*, 1840.
[31] C. Zhang, Y. Shi, L. Shi, H. Li, R. Li, S. Hong, S. Zhuo, T. Zhang, P. Wang, *Nat. Commun.* **2021**, *12*, 998.
[32] Y. Zhang, T. Xiong, L. Suresh, H. Qu, X. Zhang, Q. Zhang, J. Yang, S. C. Tan, *ACS Energy Lett.* **2020**, *5*, 3397.
[33] A. T. Liu, G. Zhang, A. L. Cottrill, Y. Kunai, A. Kaplan, P. Liu, V. B. Koman, M. S. Strano, *Adv. Energy Mater.* **2018**, *8*, 1802212.
[34] D. K. Nandakumar, Y. Zhang, S. K. Ravi, N. Guo, C. Zhang, S. C. Tan, *Adv. Mater.* **2019**, *31*, 1806730.
[35] S. Guo, X. Dai, X. Chen, Y. Lei, J. Shi, B. Tong, Z. Cai, Y. Dong, *ACS Mater. Lett.* **2021**, *3*, 379.
[36] K. S. Moreira, D. Lermen, L. P. dos Santos, F. Galembeck, T. A. L. Burgo, *Energy Environ. Sci.* **2021**, *14*, 353.

[37] Y. Huang, H. Cheng, C. Yang, H. Yao, C. Li, L. Qu, *Energy Environ. Sci.* **2019**, *12*, 1848.

[38] A. T. Liu, Y. Kunai, A. L. Cottrill, A. Kaplan, G. Zhang, H. Kim, R. S. Mollah, Y. L. Eatmon, M. S. Strano, *Nat. Commun.* **2021**, *12*, 3415.

[39] X. Li, J. Li, J. Lu, N. Xu, C. Chen, X. Min, B. Zhu, H. Li, L. Zhou, S. Zhu, T. Zhang, J. Zhu, *Joule* **2018**, *2*, 1331.

[40] Y. Wu, R. Kong, C. Ma, L. Li, Y. Zheng, Y. Lu, L. Liang, Y. Pang, Q. Wu, Z. Shen, H. Chen, *Energy Environ. Mater.* **2022**, https://doi.org/10.1002/eem2.12251.

[41] J. Bae, M. S. Kim, T. Oh, B. L. Suh, T. G. Yun, S. Lee, K. Hur, Y. Gogotsi, C. M. Koo, I.-D. Kim, *Energy Environ. Sci.* **2022**, *15*, 123.

[42] J. R. Schroeder, K. D. Beyer, *J. Phys. Chem. A* **2016**, *120*, 9948.

[43] J. Xu, T. Li, T. Yan, S. Wu, M. Wu, J. Chao, X. Huo, P. Wang, R. Wang, *Energy Environ. Sci.* **2021**, *14*, 5979.

[44] A. Alizadeh, M. Wang, *Electrophoresis* **2020**, *41*, 1067.

[45] C. Masarapu, H. F. Zeng, K. H. Hung, B. Wei, *ACS Nano* **2009**, *3*, 2199.

[46] J. Bae, T. G. Yun, B. L. Suh, J. Kim, I.-D. Kim, *Energy Environ. Sci.* **2020**, *13*, 527.

[47] Y. Zhang, A. Narayanan, F. Mugele, M. A. Cohen Stuart, M. H. G. Duits, *Colloids Surf. A Physicochem. Eng. Asp.* **2016**, *489*, 461.

[48] M. A. Brown, A. Goel, Z. Abbas, *Angew. Chem., Int. Ed.* **2016**, *55*, 3790.

[49] J. Zhao, W. Zhu, X. Wang, L. Liu, J. Yu, B. Ding, *ACS Nano* **2020**, *14*, 1045.

[50] J. Yin, J. Zhou, S. Fang, W. Guo, *Joule* **2020**, *4*, 1852.